Abstract

Purpose – This paper aims to investigate the impact of three different flow channel cross-sections on the performance of the fuel cell.

Design/methodology/approach – A comprehensive three-dimensional polymer electrolyte membrane fuel cell model has been developed and a set of conservation equations have been solved. The flow is assumed to be steady, fully developed, laminar, isothermal and incompressible. The investigated cross-sections are the commonly-used square cross-section, the increasingly used trapezoidal cross-section and a novel hybrid configuration where the cross-section is square at the inlet and trapezoidal at the outlet.

Findings – The results show that a slight gain is obtained when using the hybrid configuration and this is due to increased velocity which improves the supply of the reactant gases to the catalyst layers and removes heat and excess water more effectively compared to other configurations. Further, the reduction of the outlet height of the hybrid configuration leads to even better fuel cell performance and this is again due to increased velocity in the flow channel.

Practical implications – The data generated in this study will be highly valuable to engineers interested in studying the effect of fluid cross-sectional shape on fuel cell performance.

Originality/value – This study proposes a novel flow field with variable cross-section. This design can supply a higher amount of reactant gases to the catalyst layers, dissipates heat and remove excess water more effectively.

1. Introduction

Polymer electrolyte membrane (PEM) fuel cells have been increasingly used in a multitude of portable, automotive and stationary applications and this is due their high efficiency and low-temperature operation (Shimizu, Sepunaru and Compton, 2016). However, PEM fuel cell technology needs to be even more efficient to compete with the conventional power conversion technologies (Özgür and Yakaryılmaz, 2018). Among them, the uniformity of reactants in the flow field of the PEM fuel cell is a key issue that needs to be considered, because it can affect the uniformity of the current density distribution, heat distribution, and water distribution and transfer (Al-Baghdadi and Al-Janabi, 2007). Flow-field plates (also know as bipolar plates) are one of the key components for PEM fuel cells. They are, through hosting the grooves or the flow channels, mainly responsible for supplying reacting gases to the catalyst layers (where the half-reactions take place) through the gas diffusion layers (GDLs). They also assist in: (i) removing excess water from the heart of the fuel cell, which is the membrane electrode assembly (MEA), and (ii) electrically connecting between the anodes and the cathodes of the cells in a fuel cell stack. The impact of the shape of the cross-section of the flow channel has been extensively investigated in the literature.

Carcadea et al. (Carcadea *et al.*, 2021) investigated the effect of the depth of the flow channel on the performance of the fuel cell. They found that the maximum current density increased by around 7% with the smallest depth and this is due to better removal of excess water and better membrane humidification. Yan et al. (Wang, Duan and Yan, 2007) showed that the best fuel cell performance is obtained with a height taper ratio of 0.5 and a width taper ratio of 1.8 and this is due to the improved fuel utilisation efficiency and water removal. Fontana et al. (Fontana

et al., 2011) investigated the impact of the inclination of the flow channel and they found that the peak power density increases by 8% with an inclination of 0.75°. Kumar and Reddy developed a numerical model to study the influence of different cross-sectional shapes of the flow field on the performance of PEM fuel cell. They showed that the triangular and semi-circular cross-sections can increase the hydrogen consumption rate by up to 9% (Kumar and Reddy, no date). Zeng et al. optimised the cross-sectional shape of fuel cell channels by using a genetic algorithm. In this study, the width of the bottom and the top edges of the channel were the variables and the output power of the fuel cell was the objective function. The fuel cell had the best performance when the width of the bottom and the top edges of the trapezoidal channel were around 1.3 mm and 0.9 mm respectively. Namely, at 0.5 V, the output power of the optimised design was found to be around 8 % higher than that of the conventional square flow channel. This is due to the fact that the optimised design provides a larger contact area between the flow channel and the gas diffusion layer, resulting in higher and more uniform supply of reactant gases to the catalyst layer (Zeng *et al.*, 2017).

Liu et al. (Liu *et al.*, 2017) used genetic algorithm to optimise the channel structure of PEM fuel cell. The variables in the study were the heights of the inlet and the outlet of the channel. The output power were the objective function and used to evaluate the fuel cell performance. The best performance was obtained for the conical channel with inlet height of ~ 0.39 mm and outlet height of 0.20 mm. This is because this conical structure, relative to other configurations, provides a higher pressure increase along the channel, thus reducing the mass transfer resistance.

Ahmed et al. (Ahmed and Sung, 2006) numerically studied three different channel cross-sections: rectangular, trapezoidal, and parallelogram on the PEM fuel cell performance. Their

results showed that the distribution of the reactant gas becomes more uniform at the interface between the cathode GDL and the membrane as the width of the rib decreases, thereby assisting in reducing the mass concentration losses. The results also showed that, compared to other investigated cross-sections, the rectangular cross-section channel provides a higher cell voltage, while the trapezoidal cross-section achieves a more uniform current density distribution at the interface between the cathode GDL and the membrane. Owejan et al. (Owejan *et al.*, 2007) experimentally investigated the influence of rectangular and triangular cross-sections on the PEM fuel cell performance. The study showed that there is less water accumulated in rectangular channels than in triangular channels of the same cross-sectional area as more water is retained at the corners of the triangular channels adjacent to the GDL. Wang et al. (Wang, Duan and Yan, 2007) numerically studied the influence of the flow channel area ratio, which is the ratio between the cathode flow channel area to the total reaction area, on the fuel cell performance. Their study shows that, for both parallel and interdigitated flow configurations, the larger is the flow channel area ratio, the better is the fuel cell performance and this is mainly due to the increase in the contact area between the reactant gas and the GDL. However, the impact of this parameter (i.e. the flow channel area ratio) is less with the interdigitated flow configuration and this is because the baffle configuration already forces the reactant gas to enter the GDL and subsequently the catalyst layers. Higier and Liu (Higier and Liu, 2010) locally measured the current under the rib and channel in a variety of single pass serpentine flow fields of a PEM fuel cell. They showed that any optimum flow fields should have narrow channels.

Metallic flow-field plates have been increasingly used and this is due to ease of manufacture and their superior mechanical strength compared to the conventionally-used graphitic flow-

field plates (Karimi *et al.*, 2012). These metallic plates are normally produced through stamping or hydroforming processes which result in trapezoidal flow channels (Xu *et al.*, 2016). Ismail et al. (Ismail *et al.*, 2021) numerically investigated the impact of some geometrical parameters including the sidewall angle on the key flow characteristics including the Poiseuille number and the incremental pressure drop. They found that the impact of the rounded corners could not be overlooked for very low channels heights or very high sidewall angles. Nima Ahmadi et al. found that the humidity of the inlet gas and membrane water management are the most important parameters that affect the performance and mass transfer of fuel cells (Ahmadi et al., 2013). Hossein Samanipour and his research team reported a new cylindrical polymer fuel cell, and the results showed that the cylindrical fuel cells have the best capacity (Samanpour, Ahmadi and Jabbary, 2022). Hojjat Ashrafi et al. reported that the serpentine gas channels have a higher current density and output power compared to the parallel gas channels, and also generate less liquid water than parallel gas channels (Ashrafi et al., 2022).

Although the influence of the gas channel configurations on the performance of the PEM fuel cells has been thoroughly investigated by Nima Ahmadi et al. (Ahmadi and Kõrgesaar, 2020), (Ahmadi et al., 2011), in this paper some new and important improvements and optimizations of the flow channel geometry have been made. In this paper, we have developed an important, accurate and comprehensive three-dimensional multiphase numerical model that combines the conventional square gas flow channel and trapezoidal flow channel. The proposed new 'hybrid' configuration flow channel has a decreasing cross-section along the gas flow direction. Unlike the nozzle-shaped gas channel proposed by Nima Ahmadi et al. (Ahmadi et al., 2018), and the 'hybrid' flow channel retains the boundary area between the flow channel and the GDL. This

not only increases the gas velocity but also enables better reactant exchange and enhances the water removal.

2. Model description

The computational domain of the base case or Case 1 (where the cross-section of the channel is square) of the modelled fuel cell is shown in Figure 1. As shown in the figure, only a portion of the fuel cell which incorporates a single straight channel for each side of the fuel cell (the cathode and the anode) has been modelled in order to save the computation time. The dimensions of the computational domain are 50 mm × 2 mm × 3.47 mm.

The main assumptions considered in the study are that:

(i) The operation of the fuel cell is steady state.
(ii) The flow in the channels is laminar and incompressible since the Reynolds number is small.
(iii) The gases mixture are considered as an ideal gas.
(iv) The GDL, the CL layer and the membrane electrolyte are all isotropic.

The other two computation cases investigated in this study are the modelled fuel cell with (a) trapezoidal channels (Figure 2a) which have the same cross-sectional areas as the square channels (the width of the smaller base is 0.5 mm and the height of the channel is 1mm) and (b) hybrid channels where the cross section at the inlets of the channels is square and trapezoidal at the outlets (Figure 2b). The cross-sectional area in the latter design continually decreases from the inlet to the outlet. It should be noted that the same flow channel flow configurations were maintained for both the cathode and the anode sides of the fuel cell.

[Figures 1 and 2]

2.1. Governing equations

The following conservation equations have been used in the model. The conservation of mass, or the continuity equation, is given by (Afshari and Jazayeri, 2010), (Jiao and Li, 2009), (Ahmadi et al., 2018):

$$\nabla \cdot \rho \vec{u} = 0 \tag{1}$$

Where ρ is the density of the fluid, and $\vec{u}$ is the velocity vector.

The conservation of momentum equation is given as follows (Afshari and Jazayeri, 2010), (Ahmadi et al., 2018):

$$\nabla(\rho \vec{u}\vec{u}) = -\nabla p + \nabla(\mu \nabla \vec{u}) + S_u \tag{2}$$

Where p is the fluid pressure, μ is the dynamic viscosity, and S_u is the momentum source term. The conservation of species may be expressed as follows (Carcadea et al., 2018), (Ahmadi et al., 2018):

$$\nabla(\vec{u} Y_{ij}) = \nabla\left(D_{ij}^{eff} \nabla Y_i\right) + S_i \tag{3}$$

Where Y_i is the mass fraction of the species i, D_i^{eff} is the effective mass diffusion coefficient of the species i into j, and S_i is the source term of the species i (O_2, H_2 or H_2O) which is given in Table 3.

The energy transport equation could be expressed as follows (Carcadea *et al.*, 2018):

$$\nabla \cdot \left(\rho c_p \vec{u} T\right) = \nabla(k \nabla T) + S_T \tag{4}$$

Where ρ is the density of the fluid is, $\vec{u}$ is the velocity vector, k is thermal conductivity, S_T is the thermal source term which is listed in Table 3. Conservation of charge equations are obtained as follows (Carcadea *et al.*, 2018):

$$\nabla(\sigma_c \nabla \emptyset_c) = S_c \tag{5}$$

$$\nabla(\sigma_{mem} \nabla \emptyset_{mem}) = S_{mem} \tag{6}$$

$$\sigma_m = (0.514\lambda - 0.326) \cdot \exp(1268 \cdot (\frac{1}{303} - \frac{1}{T})) \tag{7}$$

Where σ_c and σ_m are respectively the electrical and the ionic conductivities, $\emptyset_c$ and $\emptyset_m$ are respectively the electrical and protonic potentials, λ is the dissolved water content. S_c and S_m are the charge source terms and are equal to the volumetric current density obtained by the Butler-Volmer equation [17]:

$$J_a = i_a^{ref} \zeta_{eff} \left(\frac{P_{H_2}}{C_{H_2}^{ref} H_{H_2}}\right)^{0.5} \left(exp\left(\frac{\alpha_a F}{RT}\eta_a\right) - exp\left(\frac{-\alpha_c F}{RT}\eta_a\right)\right) \tag{8}$$

$$J_c = i_c^{ref} \zeta_{eff} \left(\frac{P_{O_2}}{C_{O_2}^{ref} H_{O_2}} \right)^{0.5} \left(-exp\left(\frac{\alpha_a F}{RT} \eta_c \right) + exp\left(\frac{-\alpha_c F}{RT} \eta_c \right) \right) \quad (9)$$

Where i^{ref} is the reference exchange current density of a unit active surface area, ζ_{eff} is the active surface area, C^{ref} is the reference value of the local species concentration, α is the charge transfer coefficient for either the cathode or the anode electrode, and F is Faraday's constant. η_a and η_c are the anodic and cathodic overpotentials and are obtained using the following expressions:

$$\eta_a = \phi_s - \phi_{mem} \quad (10)$$

$$\eta_c = \phi_s - \phi_{mem} - V_{oc} \quad (11)$$

Where V_{oc} is the open –circuit potential (Li *et al.*, 2017):

$$V_{oc} = 1.229 - 8.456 \times 10^{-4}(\mathrm{T} - 298.15) + 4.31 \times 10^{-5}\mathrm{T}\log\left(P_{H_2} P_{O_2}^{0.5}\right) \quad (12)$$

The water in a PEM fuel cell have three phases: gaseous, liquid, and dissolved. The conservation of dissolved water could be expressed as follows (Carcadea *et al.*, 2018):

$$\nabla \cdot \left(\vec{\imath}_m \frac{n_d}{F} M_{H_2 o} \right) = \nabla\left(M_{H_2 o} D_w \nabla\lambda \right) + S_\lambda + S_{gd} + S_{ld} \quad (13)$$

where λ is water content, n_d the is osmotic drag coefficient, D_w is the diffusion coefficient, S_λ is the water generation rate at the cathode catalyst layer, S_{gd} is the change rate of water between the gaseous and dissolved phases, S_{ld} is the change rate of water between the liquid and

dissolved phases. The mathematical definitions for all the source terms are presented in Table 3. The osmotic drag coefficient is given as follows (Springer, Zawodzinski and Gottesfeld, 1991):

$$n_d = \frac{2.5\lambda}{22} \tag{14}$$

The diffusion coefficient of water content is obtained as follows (Springer, Zawodzinski and Gottesfeld, 1991):

$$D_w^m = \frac{\rho_m}{EW} \cdot M_{H_2O} D_l \nabla\lambda \tag{15}$$

Where ρ_m and EW are the membrane dry density and membrane equivalent weight. The membrane water diffusivity is given as follows:

$$D_l = f(\lambda) e^{2416(\frac{1}{303}-\frac{1}{T})} \tag{16}$$

Where $f(\lambda)$ is defined as follows:

$$f(\lambda) = \begin{cases} 10^{10} & \lambda < 2 \\ 10^{10}\lambda\left(1 + 2(\lambda - 2)\right) & 2 \le \lambda \le 3 \\ 10^{10}\lambda\left(3 - 1.67(\lambda - 3)\right) & 3 \le \lambda \le 4.5 \\ 1.25 \times 10^{10}\lambda\left(3 - 1.67(\lambda - 3)\right) & 4.5 \le \lambda \end{cases} \tag{17}$$

Water content is expressed as follows:

$$\lambda = \begin{cases} 0.043 + 1718a - 39.85a^2 + 36a^2 & (a < 1) \\ 14 + 1.4(a - 1) & (a > 1) \end{cases} \quad (18)$$

1 Water activity, a, is given as follows:

$$\mathrm{a} = \frac{P_{wv}}{P_{sat}} + 2s \quad (19)$$

2 where s is saturation of water vapour and P_{wv} is water vapour pressure:

$$P_{wv} = \chi_{H_2O} P \quad (20)$$

3 P_{sat} is saturation pressure:

$$\log_{10} P_{sat} = -2.1794 + 0.02953 \cdot (T - 273.15) - 9.1837 \cdot 10^{-5} \cdot (T - 273.15)^2 + 1.4454 \cdot 10^{-7} \cdot (T - 273.15)^3 \quad (21)$$

4 The impact of the liquid water on the operation of the fuel cell is accounted for by using the
5 conservation of water saturation equation (Carcadea *et al.*, 2018):

$$\nabla \cdot \left(\frac{\rho_l K K_r}{\mu_l} \nabla (P_c + \mathrm{p}) \right) = S_{gl} \quad (22)$$

6 Where μ_l is the dynamic viscosity of liquid water, P_c is the capillary pressure of the liquid
7 water and K is the absolute permeability. S_{gl} is the mass change rate between the gas and liquid

phases; its mathematical expression is shown in Table 3. K_r is the relative permeability and is given as follows:

$$K_r = \begin{cases} \dfrac{\frac{M_{H_2O}}{\rho_l}\lambda_{s=1} + \frac{EW}{\rho_i}}{\frac{M_{H_2O}}{\rho_l}\lambda + \frac{EW}{\rho_i}} & in\ the\ membrane \\ s & in\ the\ GDL\ and\ the\ CLs \end{cases} \tag{23}$$

P_c is the capillary pressure and is given as follows:

$$P_c = \begin{cases} \sigma\cos(\theta)\left(\frac{\varepsilon}{K}\right)^{\frac{1}{2}} 1.417(1-s) - 2.12(1-s)^2 + 1.263(1-s)^3 & (\theta < 90°) \\ \sigma\cos(\theta)\left(\frac{\varepsilon}{K}\right)^{1/2} 1.417s - 2.12s^2 + 1.263s^3 & (\theta > 90°) \end{cases} \tag{24}$$

σ denotes the surface tension and θ is the contact angle.

D_{ij}^{eff} shown in Eq.3 earlier is calculated as follows: (Li *et al.*, 2017)

$$D_{ij}^{eff} = (1-s)^{1.5}\varepsilon^{1.5})(\frac{1}{D_{i,m}} + \frac{1}{D_{Kn}})^{-1} \tag{25}$$

$$D_{i,m} = D_i^{ref}(\frac{101325}{P})(\frac{T}{300})^{1.5} \tag{26}$$

$$D_{Kn} = \frac{1}{3}d_{pore}(\frac{8RT}{\pi M})^{0.5} \tag{27}$$

In this equation d_{pore} in this equation is defined as 0.2 μm.

[Tables 1 and 2]

2.2. Boundary conditions and numerical procedure

The inlet boundary conditions, in terms of the mass fractions, temperatures, and relative humidity, are listed in Table 3. In addition, the zero temperature flux, $\frac{\partial T}{\partial x} = 0$ and concentrations of the chemical species and zero-gauge pressures are set at the outlets of the flow channels. On the terminal at both sides of the wall of the channel, the solid phase potential is set to the ground potential, $\Phi_s = 0$ at the anodic terminal and it is set to the cell voltage, $\Phi_s = V_{cell}$ (a value between 0.4 V and the open circuit voltage) at the cathodic terminal. The mass flow rate is given as follows:

$$Q_a = \frac{\xi_a M_{H_2} I_{ref} A_m}{2FY_{H_2}} \tag{28}$$

$$Q_c = \frac{\xi_c M_{O_2} I_{ref} A_m}{4FY_{O_2}} \tag{29}$$

Where ξ represent the stoichiometric ratio and I_{ref} is the reference current density. The numerical model is solved using the PEMFC model within the ANSYS Fluent 2019 R3 software. The model uses a three-dimensional multiphase approach to solve the governing equations, including species, energy, potential, momentum, water content, liquid saturation, and user-defined scalar equations. To discretize the equations spatially, a second-order upwind method is used for all equations. Three different mesh sizes were used to check for mesh-independent solutions: 100 × 15 × 50, 150 × 30 × 100 and 200 × 45 × 150 for the axes X, Y and Z. In addition, the difference in the current density at 0.5 V between the first and the second

meshes is about 1.3% and between the second and the third meshes is 0.5%. Therefore, the second mesh (150 × 30 × 100) was considered in this study to ensure both reasonable accuracy and computation time. Figure 3 shows the meshed geometry for the base case and Figure 4 shows the back views, of the meshed geometries for the investigated cases, case 1 and 2 have the same geometry as inlet, case 3 is the proposed hybrid design which have a rectangular inlet but trapezoidal outlet.

[Table 2 and Figures 2 and 4]

3. Results and discussion

Figure 5 shows that the modelling output in the form of the polarisation curve of the base computation case (the modelled fuel cell with square flow channels) are in reasonably good agreement with those reported by Wang et al. (Wang *et al.*, 2003), thus imparting confidence into the predictions of the new proposed model.

[Figure 3]

Influence of the cross-sectional shape of the flow channel

Figure 6 displays the polarisation curves of the simulated fuel cell with flow channels of different cross-sectional geometries, namely, square, trapezoidal, and hybrid. The results indicate that the variation in fuel cell performance is negligible for Cases 1 (square cross-section) and 2 (trapezoidal cross-section) with respect to a given cross-sectional area. This suggests that switching from a square to a trapezoidal cross-section has minimal impact on the fuel cell performance. However, Case 3 (hybrid cross-section as described in Section 2) demonstrates a slightly better performance at low cell potentials (e.g., 0.5 V) compared to

Cases 1 and 2, with the current density at 0.4 V increasing by approximately 5% upon switching from a square to a hybrid cross-section. This important improvement can be attributed to the decrease in the channel cross-section from the inlet to the outlet, which results in an increase in the channel gas velocity (Figure 7) and subsequently and importantly facilitates the supply of reactant gases (oxygen or hydrogen) to the catalyst layers via convective flow in the Gas Diffusion Layers (GDLs) and Catalyst Layers (CLs). The availability of oxygen at the cathode GDL-CL interface is also affected, with less oxygen being available for Case 3, thus indicating that more oxygen is supplied and consumed at the catalyst layer for this case. It is worth noting that the transport of species within typical GDLs, where the gas permeability is around 10-13 m^2, is dominated by diffusion (Ismail et al., 2012). This explains the minimal improvement observed in fuel cell performance with the hybrid channel cross-sections. Possible further research could investigate the impact of the hybrid channel cross-sections on other aspects of the fuel cell performance, such as the water management and durability.

[Figures 4, 7 and 8]

Table 4 presents the pressure drop data obtained for the different channel cross-sections investigated. It is interesting and important to note that the results reveal that the use of the hybrid cross-sections leads to an increase in the pressure drop along the cathode channel, which promotes higher convective flow rates and, subsequently, better heat and excess water removal. This is demonstrated by the temperature difference along the channel and the water concentration at the exit of the cathode channel, both of which show an improvement when using the hybrid cross-sections compared to the other cases investigated. In addition, the average temperature difference along the channel increased by 0.05°C when switching from the square to the hybrid cross-sections. Similarly, the liquid water exiting the cathode channel

increased when using the hybrid cross-sections compared to the square or trapezoidal cross-sections. Comparable observations can be made for the anode flow channels (not shown), although the effect is less pronounced due to the lower flow rates used in those channels. Moreover, Table 4 shows that the use of trapezoidal cross-sections results in a slightly higher pressure drop along the channel compared to the square cross-sections, thereby improving the heat dissipation and excess water removal. Also, the temperature difference and water concentration at the channel exit for trapezoidal cross-sections are comparable to those of the hybrid cross-sections. These findings confirm the important hypothesis that switching from a square to a trapezoidal cross-section has a positive impact on the fuel cell performance and other key performance indicators.

[Table 3]

Influence of the outlet height

The modelled fuel cell with hybrid flow channels shows slightly better performance than those with square or trapezoidal flow channels. However, to further improve the performance of the fuel cell, the height of the outlet of the hybrid channel has been varied from the original case of 1 mm to 0.75, 0.50, and 0.25 mm. Figure 9 shows that the limiting current density increases slightly as the outlet height decreases. Specifically, the current density at 0.4 V increases by about 6% when the channel height decreases from 1 to 0.25 mm. According to the Bernoulli's principle, as the cross-sectional area of the flow channel decreases, and the mass flow rate remains constant, the velocity has to increase to maintain the same mass flow rate. Thus this nozzle like configuration will increase the velocity of the gas flow, which is beneficial to the reactant to transport to the reaction area. In addition, high speed flow can increase the

magnitude of the diffusion term in the species conservation equation, which describes how molecules move and diffuse through the gas channel. This can intern affect the convection term of the equation, which describes the transport of the molecules due to the bulk flow of the gas. As shown in Figure 10, the velocity magnitude increases significantly when the height of the channel decreases in the direction of gas flow, which enhanced the reactant distribute more uniformly and helps reactant to reach the reaction site, as shown in Figure 11. The latter figure demonstrates that the concentration of oxygen at the interface between the cathode GDL and the CL decreases as the channel height decreases, indicating that more oxygen is supplied to and consumed at the catalyst layer. This suggests that decreasing the channel height can improve the performance of the fuel cell. However, it is important to note that decreasing the channel height can also increase the pressure drop along the channel, which may have negative effects on the performance of the fuel cell, and should be considered in further optimization investigations.

[Figures 9, 10 and 11]

Table 5 presents the impact of the outlet height on the additional key performance indicators of the modelled fuel cell. The table shows that as the outlet height decreases from 1 to 0.25 mm, the pressure drop along the cathode flow channel increases almost fourfold, and this is primarily due to the increase in the gas velocity. This increase in velocity improves the heat dissipation and excess water removal. Specifically, the difference in the temperature between the inlet and outlet of the cathode channel, averaged across the channel, increases by 0.77 °C, and the amount of liquid water exiting the cathode flow channel slightly increases from 0.0154 to 0.0157 kmol/m^3. However, it should be noted that the increased pressure drop requires

relatively high pumping power to maintain the flow rate, which can decrease the system efficiency and increase the costs. Therefore, optimizing the pressure drop along the flow channels in real-life fuel cell systems is critical to ensure both acceptable efficiency and cost-effectiveness. It is worth mentioning that these findings demonstrate the significance and importance of considering multiple key performance indicators when evaluating the performance of a fuel cell, rather than focusing on a single indicator. By doing so, researchers can obtain a more comprehensive understanding of the performance of the fuel cell and provide deeper insights into how to improve its efficiency and effectiveness.

[Table 4]

4. Conclusions

A comprehensive three-dimensional numerical model has been created for a polymer electrolyte membrane fuel cell. This has been performed to investigate the impact of switching from a commonly used square flow channel cross-section to increasingly-used trapezoidal cross section and a hybrid cross-section (where the cross-section at the inlet is square and the cross-section at the outlet is trapezoidal) on the global and local performance of the fuel cell. The results show that the fuel cell with hybrid flow channel cross-sections generally perform better than other configurations, particularly at high current densities. Namely, the current density increased by around 5% at 0.4 V when switching to hybrid configuration. This is attributed to the increased velocity in the hybrid flow channel (due to gradually decreasing cross-section from the inlet to the outlet) which is responsible for supplying higher amount of reactant gases to the catalysts layers. Further, this hybrid configuration, compared to other configurations, results in better heat dissipation and removal of excess water. Furthermore,

reducing the height of the outlet of the hybrid cross section demonstrates a better fuel cell performance. For example, reducing the height of the outlet from 1 to 0.25 mm for this configuration results in an increase in the current density at 0.4 V by 6%. As with the first investigation, this is evidently due to increased velocity with decreasing outlet height which brings more amounts of reactant gases to the catalyst layers, dissipates heat and remove excess water more effectively. Due to the limited length and cos sectional area of the single channels, in future research, and this hybrid variable cross-section channel design can be applied to serpentine or parallel flow field plate, traditionally with the fixed cross-section, to study its effects on the reactant transport, water removal, and overall performance. By applying the 'hybrid' variable cross-section channel design to these flow field plates, researchers can gain insights into how this design impacts reactant transport, water management, and overall performance. This work then can be used to improve the design and operation of fuel cell, ultimately leading to more efficient and sustainable energy generation.

Nomenclature

c_p	Specific heat capacity, J/(kg.K)
D_k^{eff}	Effective diffusion coefficient for species k
C_k	Concentration of species k, kg/m^3
D	Diffusion conductance at the face of the control volume
F	Faraday constant, C/mol

i	Current density, A/m^2
K	Permeability, m^2
M_k	Molecular weight of species k, kg/mol
Mw	Molecular weight, kg/mol
P	Pressure, Pa
P_{wv}	Water vapor pressure
P_{sat}	Saturation pressure
R	Universal gas constant, $Pa.m^3/(mol.K)$
$S_{s,k}$	Source term for species k
S_φ	Charge source term
S	Source term in the conservation equation
S_e	Energy source term
S_m	Mass source term
S_M	Momentum source term

T	Temperature, K
t	Time, s
V	Control volume
v	Velocity in x-direction
v	Velocity vector, m/s
Y_k	Mass fraction for species k

Greek symbols

χ	Molar fraction
δ	The thickness of porous medium, m
ε	Porosity of the porous medium.
$\emptyset$	General variable in the conservation equation
φ_m	Electrolyte phase potential, V
φ_s	Solid phase potential, V
$\boldsymbol{\Gamma}$	Diffusion coefficient in the conservation equation

λ	Water content
μ	Fluid viscosity, Pa.s
ρ	Density, kg/m^3

Subscripts

Unless stated otherwise, all the subscripts in this thesis are given as follows:

k	Species k
eff	Effective value
o	Reference
eff	Effective value

Abbreviations

CFD	Computational fluid dynamics
GDL	Gas diffusion layer
MEA	Membrane electrode assembly
PEMFC	Proton exchange membrane fuel cell

Chemical symbols

CO_2	Carbon dioxide
H^+	Proton
H_2	Hydrogen molecule
H_2O	Water molecule
O_2	Oxygen molecule

Reference:

Afshari, E. and Jazayeri, S. A. (2010) 'Effects of the cell thermal behavior and water phase change on a proton exchange membrane fuel cell performance', *Energy Conversion and Management*. Elsevier Ltd, 51(4), pp. 655–662. doi: 10.1016/j.enconman.2009.11.004.

Ahmadi, N. *et al.* (2011) 'Three-dimensional computational fluid dynamic study of effect of different channel and shoulder geometries on cell performance', *Australian Journal of Basic and Applied Sciences*, 5(12), pp. 541–556.

Ahmadi, N. *et al.* (2013) 'NUMERICAL INVESTIGATION OF THE EFFECT OF INLET GASES HUMIDITY ON POLYMER EXCHANGE MEMBRANE FUEL CELL (PEMFC) PERFORMANCE', *Transactions of the Canadian Society for Mechanical Engineering*, 37(1), pp. 12–26. doi: https://doi.org/10.1139/tcsme-2013-0001.

Ahmadi, N. *et al.* (2018) 'Study of the effect of gas channels geometry on the performance of polymer electrolyte membrane fuel cell', *Periodica Polytechnica Chemical Engineering*, 62(1), pp. 97–105. doi: 10.3311/PPch.9369.

Ahmadi, N. and Kõrgesaar, M. (2020) 'Analytical approach to investigate the effect of gas channel draft angle on the performance of PEMFC and species distribution', *International Journal of Heat and Mass Transfer*. Elsevier Ltd, 152, p. 119529. doi: 10.1016/j.ijheatmasstransfer.2020.119529.

Ahmed, D. H. and Sung, H. J. (2006) 'Effects of channel geometrical configuration and shoulder width on PEMFC performance at high current density', *Journal of Power Sources*, 162(1), pp. 327–339. doi: 10.1016/j.jpowsour.2006.06.083.

Al-Baghdadi, M. A. R. S. and Al-Janabi, H. A. K. S. (2007) 'Effect of operating parameters on the hygro-thermal stresses in proton exchange membranes of fuel cells',

International Journal of Hydrogen Energy, 32(17), pp. 4510–4522. doi: 10.1016/j.ijhydene.2007.05.007.

Ashrafi, H. *et al.* (2022) 'Introducing a new serpentine configuration of gas channels to enhance the performance and reduce the water flooding in the PEMFC', *Iranian Journal of Chemistry and Chemical Engineering*, (April). doi: 10.30492/IJCCE.2022.546616.5111.

Carcadea, E. *et al.* (2018) 'The effects of cathode flow channel size and operating conditions on PEM fuel performance: A CFD modelling study and experimental demonstration', *International Journal of Energy Research*, 42(8), pp. 2789–2804. doi: 10.1002/er.4068.

Carcadea, E. *et al.* (2021) 'Effects of geometrical dimensions of flow channels of a large-active-area PEM fuel cell: A CFD study', *International Journal of Hydrogen Energy*. Elsevier Ltd, 46(25), pp. 13572–13582. doi: 10.1016/j.ijhydene.2020.08.150.

Fontana, É. *et al.* (2011) 'Study of the effects of flow channel with non-uniform cross-sectional area on PEMFC species and heat transfer', *International Journal of Heat and Mass Transfer*, 54(21–22), pp. 4462–4472. doi: 10.1016/j.ijheatmasstransfer.2011.06.037.

Higier, A. and Liu, H. (2010) 'Optimization of PEM fuel cell flow field via local current density measurement', *International Journal of Hydrogen Energy*. Elsevier Ltd, 35(5), pp. 2144–2150. doi: 10.1016/j.ijhydene.2009.12.116.

Ismail, M. S. *et al.* (2012) 'Effects of anisotropic permeability and electrical conductivity of gas diffusion layers on the performance of proton exchange membrane fuel cells', *Applied Energy*, 95, pp. 50–63. doi: 10.1016/j.apenergy.2012.02.003.

Ismail, M. S. *et al.* (2021) 'Fully-developed laminar flow in trapezoidal ducts with rounded corners: a numerical solution and case study', *International Journal of Numerical Methods for Heat and Fluid Flow*, (375213500). doi: 10.1108/HFF-09-2021-0620.

Jiao, K. and Li, X. (2009) 'Three-dimensional multiphase modeling of cold start processes in polymer electrolyte membrane fuel cells', *Electrochimica Acta*, 54(27), pp. 6876–6891. doi: 10.1016/j.electacta.2009.06.072.

Karimi, S. *et al.* (2012) 'A review of metallic bipolar plates for proton exchange membrane fuel cells: Materials and fabrication methods', *Advances in Materials Science and Engineering*, 2012. doi: 10.1155/2012/828070.

Kumar, A. and Reddy, R. G. (no date) *Effect of channel dimensions and shape in the flow-field distributor on the performance of polymer electrolyte membrane fuel cells*.

Li, S. *et al.* (2017) 'Influence of anisotropic gas diffusion layers on transport phenomena in a proton exchange membrane fuel cell', *International Journal of Energy Research*. John Wiley and Sons Ltd, 41(14), pp. 2034–2050. doi: 10.1002/er.3763.

Liu, Z. *et al.* (2017) 'Multi-objective optimization of operating conditions and channel structure for a proton exchange membrane fuel cell', *International Journal of Heat and Mass Transfer*, 111, pp. 289–298. doi: 10.1016/j.ijheatmasstransfer.2017.03.120.

Owejan, J. P. *et al.* (2007) 'Effects of flow field and diffusion layer properties on water accumulation in a PEM fuel cell', *International Journal of Hydrogen Energy*, 32(17), pp. 4489–4502. doi: 10.1016/j.ijhydene.2007.05.044.

Özgür, T. and Yakaryılmaz, A. C. (2018) 'A review: Exergy analysis of PEM and PEM fuel cell based CHP systems', *International Journal of Hydrogen Energy*, 43(38), pp. 17993–18000. doi: 10.1016/j.ijhydene.2018.01.106.

Samanpour, H., Ahmadi, N. and Jabbary, A. (2022) 'Effects of Applying Brand-New Designs on the Performance of PEM Fuel Cell and Water Flooding Phenomena', *Iranian Journal of Chemistry and Chemical Engineering*, 41(2), pp. 618–634. doi: 10.30492/ijcce.2020.130908.4225.

Shimizu, K., Sepunaru, L. and Compton, R. G. (2016) 'Innovative catalyst design for the oxygen reduction reaction for fuel cells', *Chemical Science*. Royal Society of Chemistry, 7(5), pp. 3364–3369. doi: 10.1039/c6sc00139d.

Springer, T. E., Zawodzinski, T. A. and Gottesfeld, S. (1991) 'Polymer Electrolyte Fuel Cell', *Kobunshi*, 57(7), pp. 498–501. doi: 10.1295/kobunshi.57.498.

Wang, L. *et al.* (2003) 'A parametric study of PEM fuel cell performances', *International Journal of Hydrogen Energy*, 28(11), pp. 1263–1272. doi: 10.1016/S0360-3199(02)00284-7.

Wang, X. D., Duan, Y. Y. and Yan, W. M. (2007) 'Numerical study of cell performance and local transport phenomena in PEM fuel cells with various flow channel area ratios', *Journal of Power Sources*, 172(1), pp. 265–277. doi: 10.1016/j.jpowsour.2007.07.026.

Xu, Y. *et al.* (2016) 'Analysis of the flow distribution for thin stamped bipolar plates with tapered channel shape', *International Journal of Hydrogen Energy*. Elsevier Ltd, 41(9), pp. 5084–5095. doi: 10.1016/j.ijhydene.2016.01.073.

Zeng, X. *et al.* (2017) 'The optimization of channels for a proton exchange membrane fuel cell applying genetic algorithm', *International Journal of Heat and Mass Transfer*, 105, pp. 81–89. doi: 10.1016/j.ijheatmasstransfer.2016.09.068.

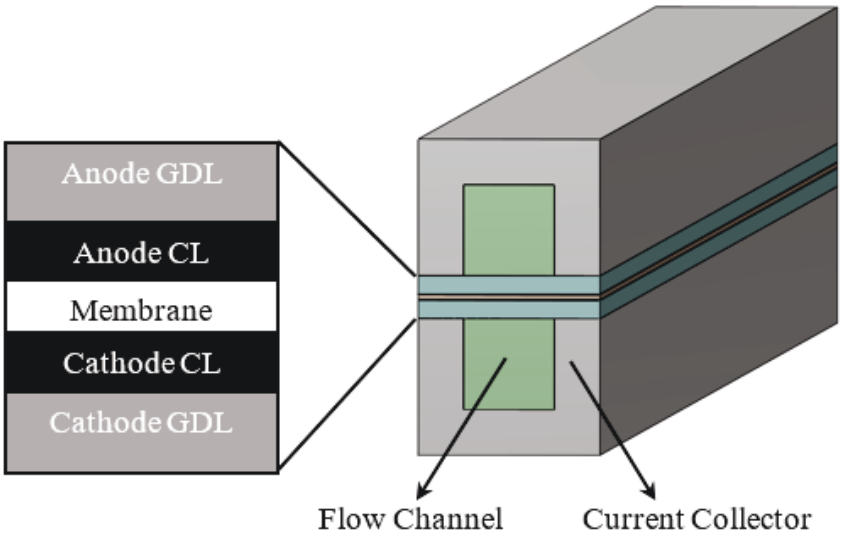

Figure 1 A schematic diagram of the base case of the PEM fuel cell model.

1

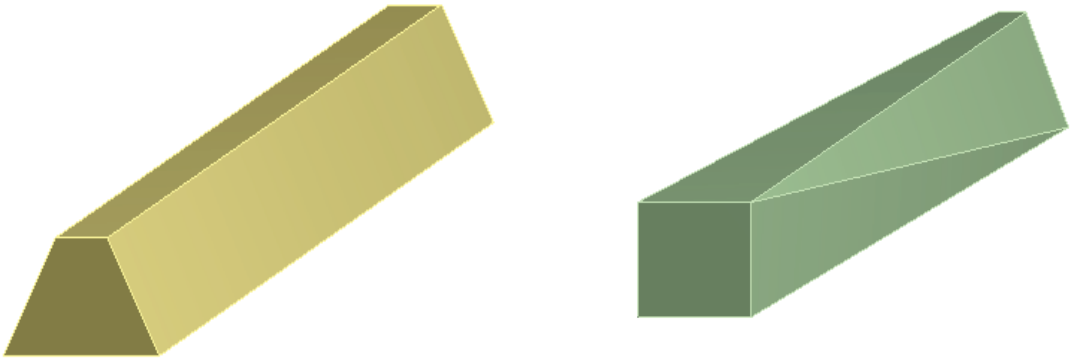

a) (b)

2 **Figure 2** Schematics for the modelled flow channels with (a) trapezoidal (Case 2), and (b) "hybrid" (Case 3) cross-
3 sections.

4

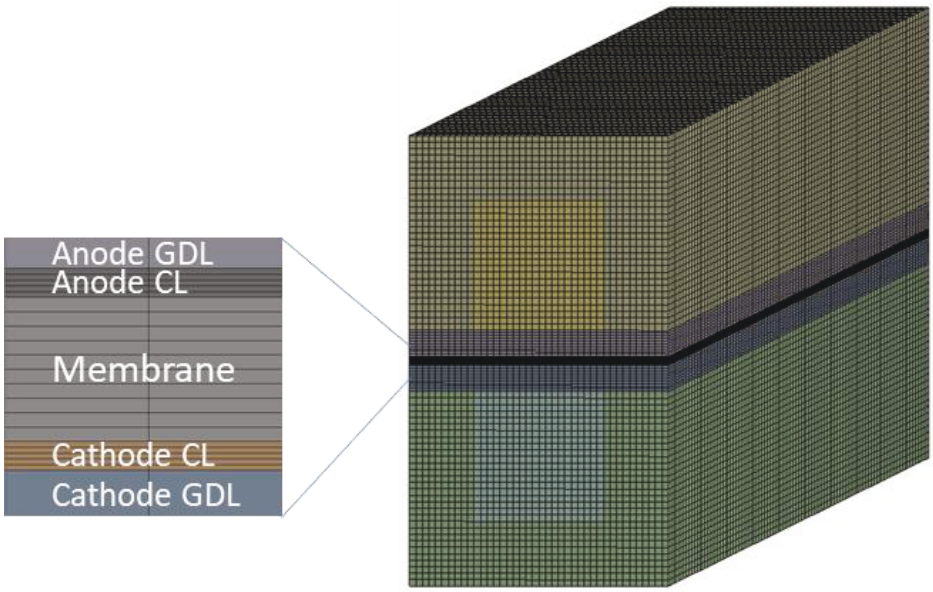

Figure 3 The meshed geometry of the base case. The zoomed-in picture shows the mesh across the membrane electrode assembly.

1

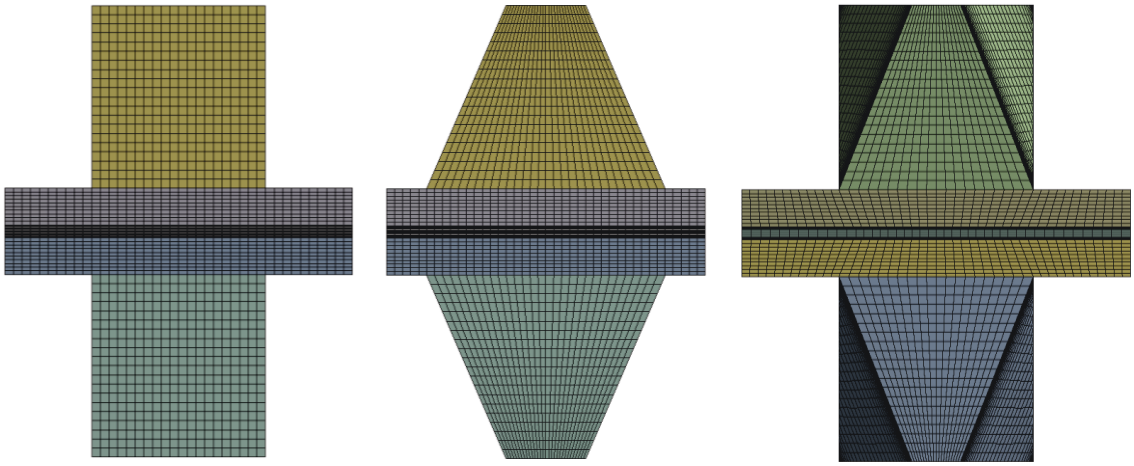

a b c

2 **Figure 4** The back view of the meshed geometries for the investigated cases (a) Case 1 (rectangular cross-section),
3 (b) Case 2 (trapezoidal cross-section), and (c) Case 3 (hybrid cross-section).

4

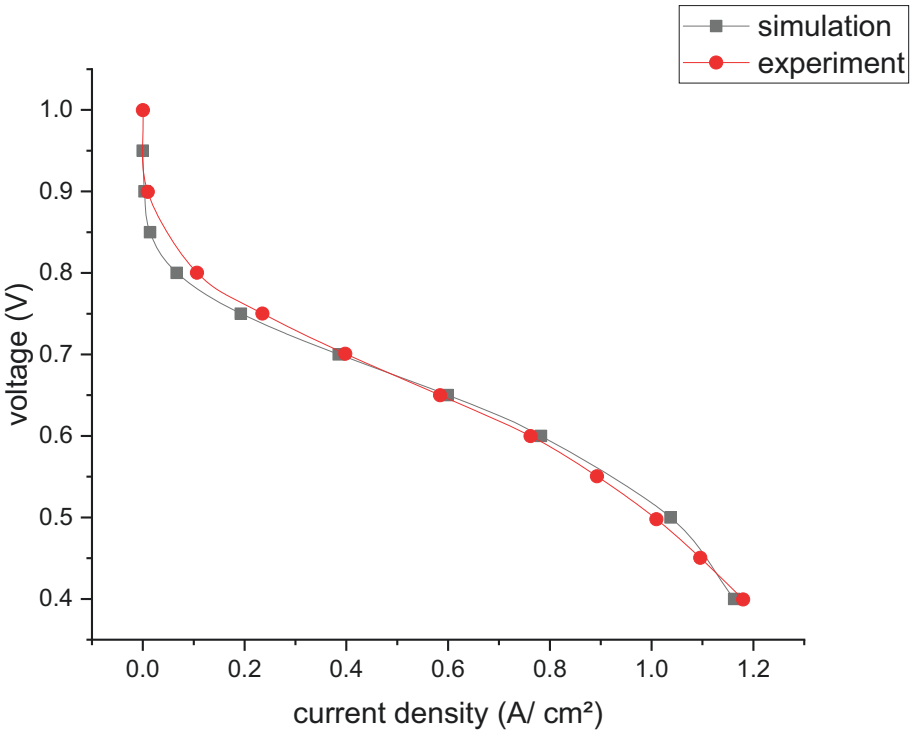

Figure 5 The polarisation curve generated by the modelled fuel cell for the base case as compared with the experimental data reported by Wang et al. [22].

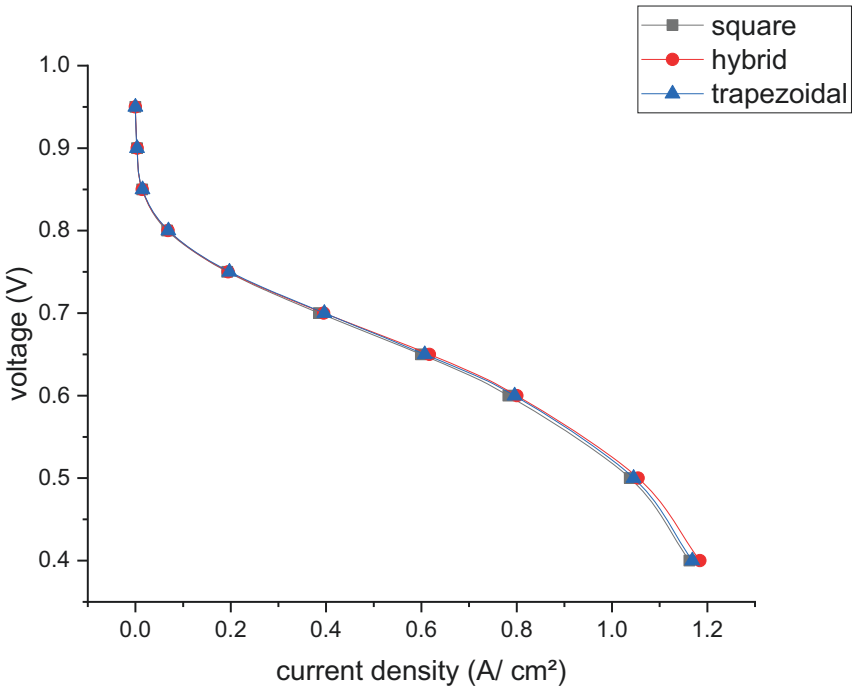

Figure 6 The polarization curves of the modelled PEM fuel cell with square, trapezoidal and hybrid flow channels.

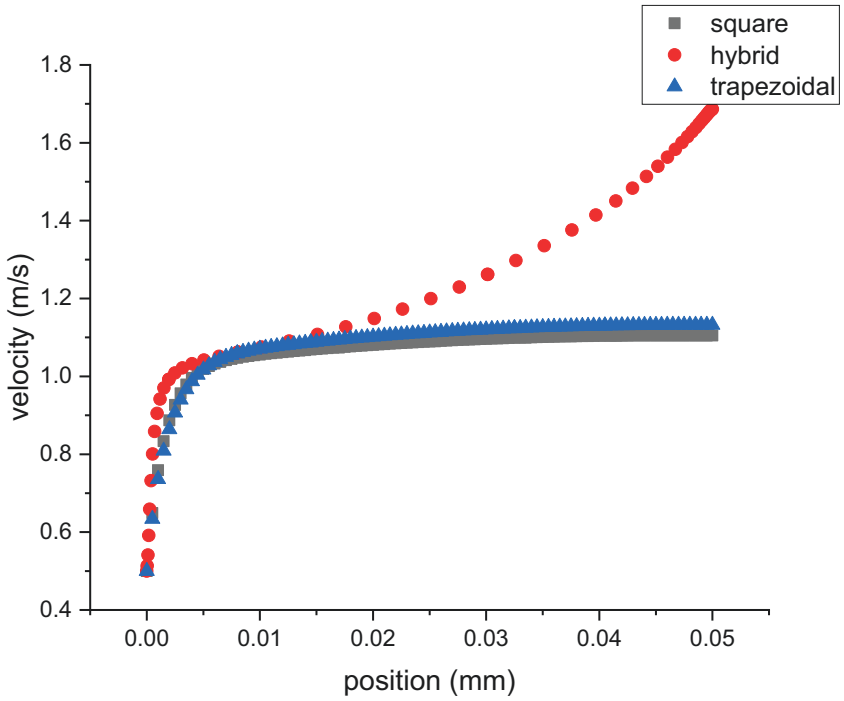

Figure 7 The velocity profile at 0.5 V along the middle line of the cathode flow channel with: rectangular, trapezoidal and hybrid cross-sections.

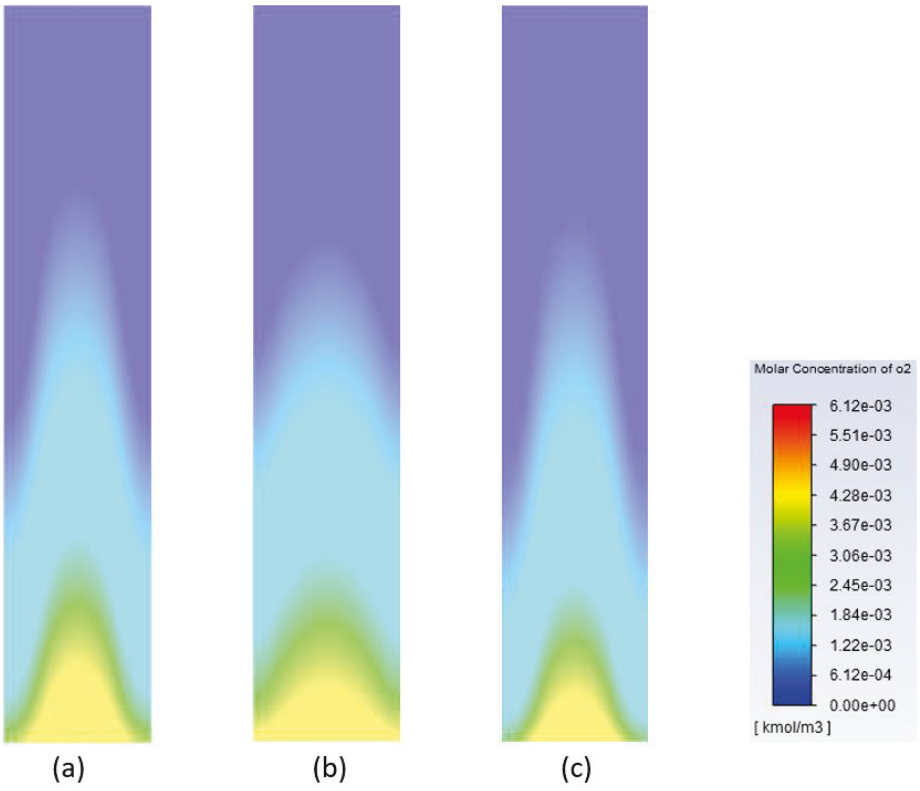

Figure 8 The contours of the oxygen concentration (kmol/m³) at the interface between the cathode CL and GDL at 0.5V with various cross-section shapes: (a) rectangular, (b) trapezoidal and (c) hybrid cross-sections.

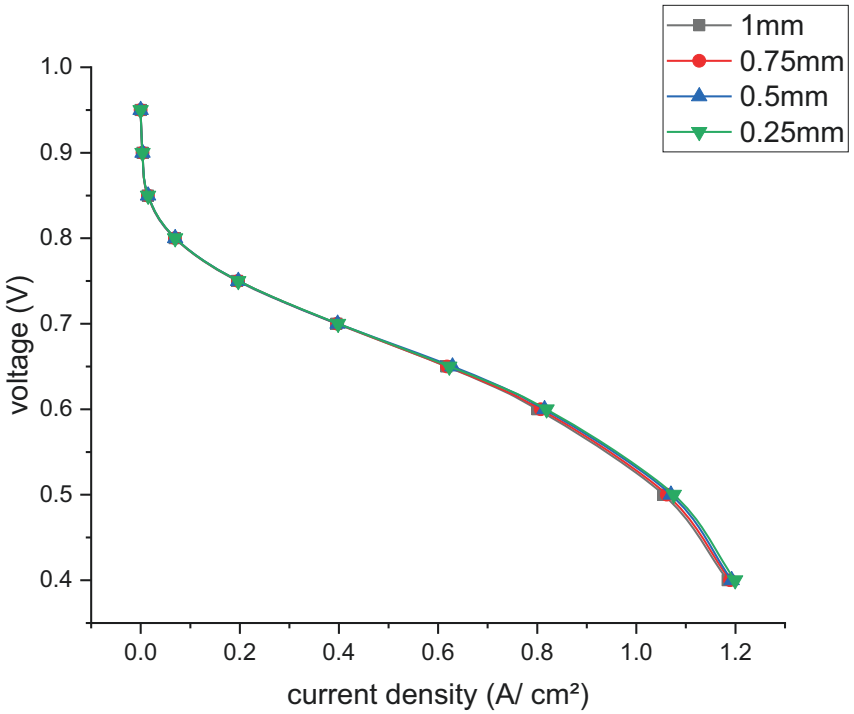

Figure 9 The polarisation curves of the modelled PEM fuel cell with varying outlet heights for hybrid channels.

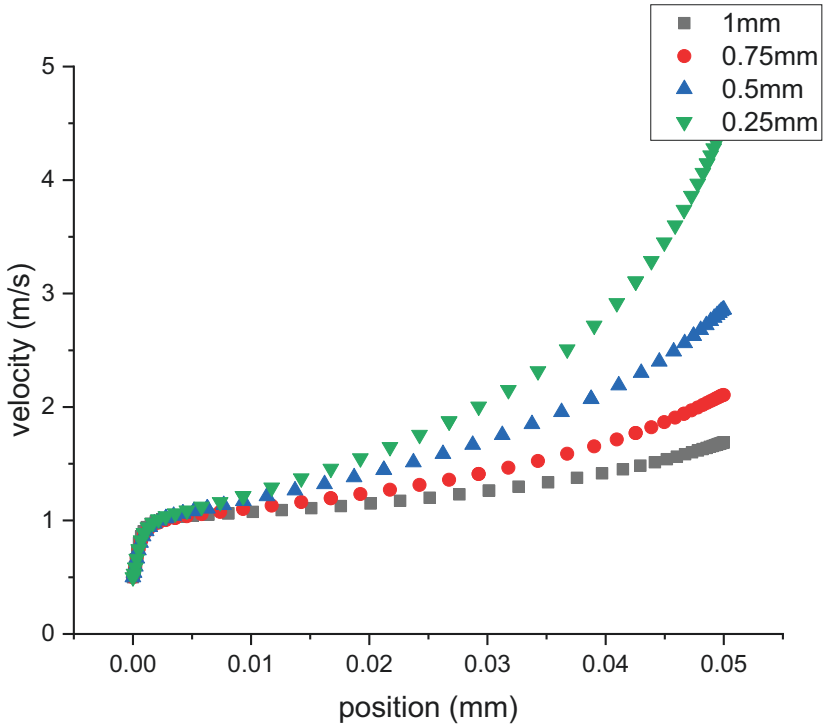

Figure 10 The velocity profiles at 0.5 V along the middle line of the hybrid cathode flow channel with varying outlet heights.

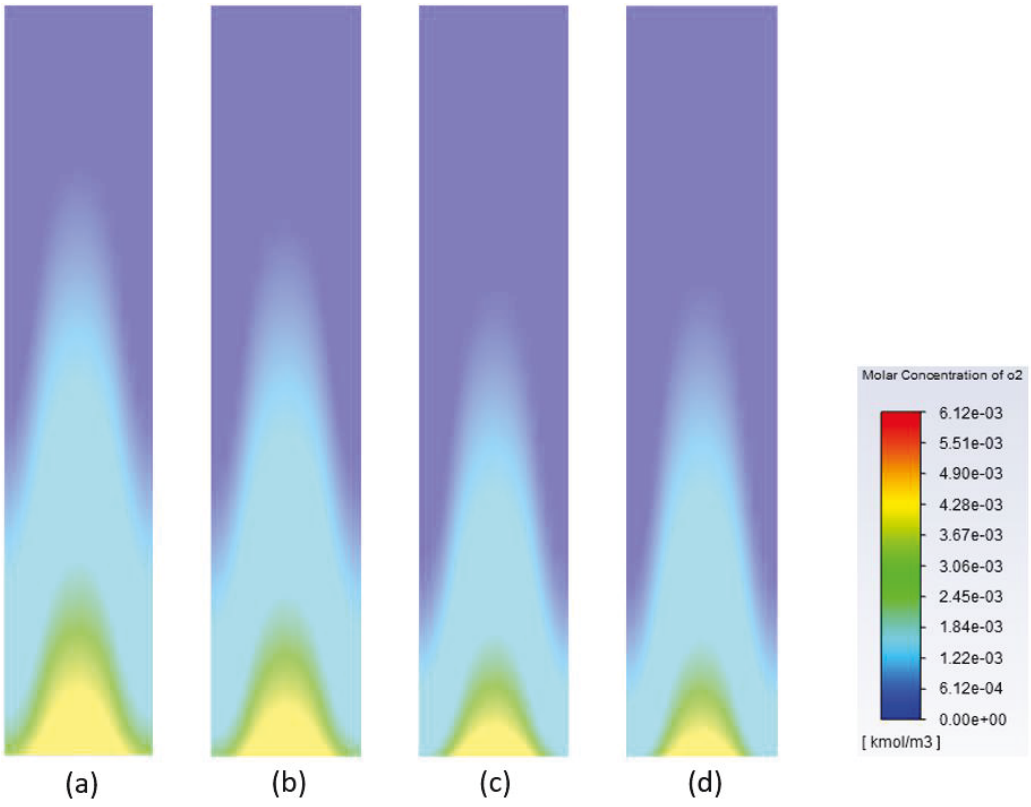

Figure 11 The contours of the oxygen concentration at the interface between the cathode GDL and the CL at 0.5V with different heights at the outlet: (a) 1.0mm, (b) 0.75mm, (c) 0.5mm and (d) 0.25mm.

1

Table 1 The parameters used in the model [19],[21],[22],[23]

Parameter	value
Reference exchange current density at anode (i_a^{ref})	6000 A/m^2
Reference exchange current density at cathode (i_c^{ref})	0.0044 A/m^2
Thickness of membrane	0.05 mm
Thickness of catalyst layer	0.01 mm
Thickness of GDL	0.2 mm
Length of channel	50 mm
Height of channel	1 mm
Width of channel	1 mm
Cathode charge transfer coefficient (α_a)	0.5
Anode charge transfer coefficient (α_c)	1
Anode/cathode specific surface area (ζ_{eff})	1×10^6
Dry membrane density (ρ_m)	1980 kg/m^3
Membrane equivalent weight (EW)	1100 kg/kmol
H_2 molar concentration ($c_{H_2}^{ref}$)	54.6×10^{-3} kmol/m^3
O_2 molar concentration ($c_{O_2}^{ref}$)	3.39×10^{-3} kmol/m^3
Porosity of anode/cathode CL (ε)	0.4
Porosity of anode/cathode GDL (ε)	0.7
GDL/CL permeability (K)	$3 \times 10^{-12}/2 \times 10^{-13} m^2$
GDL/CL contact angle (θ)	110/95°
Hydrogen diffusion coefficient (D_{H_2})	$9.15 \times 10^{-5}\ m^2/s$
Oxygen diffusion coefficient (D_{O_2})	$2.2 \times 10^{-5}\ m^2/s$
Nitrogen diffusion coefficient (D_{N_2})	$2 \times 10^{-5}\ m^2/s$
Water vapor diffusion coefficient (D_{H_2o})	$2.56 \times 10^{-5}\ m^2/s$
Thermal conductivity of CC	100 W/m/K
Thermal conductivity of GDL	21 W/m/K
Thermal conductivity of CL	0.3 W/m/K
Thermal conductivity of membrane	0.25 W/m/K
Electric conductivity of current collector (σ_{CC})	200000 S/m
Electric conductivity of gas diffusion layer (σ_{GDL})	5000 S/m

Electric conductivity of catalyst layer (σ_{CL})	2000 S/m
Hydrogen viscosity (μ)	$8.411 \times 10^{-6} Pa\ s$
Liquid water viscosity (μ)	$3.517 \times 10^{-4} Pa\ s$
Oxygen viscosity (μ)	$1.919 \times 10^{-5} Pa\ s$
Water vapour viscosity (μ)	$1.34 \times 10^{-5} Pa\ s$
Nitrogen viscosity (μ)	$1.663 \times 10^{-5} Pa\ s$
Surface tension of water (σ)	0.0625 N/m
Gas mass exchange rate γ_{gd}	0.5
liquid mass exchange rate γ_{gd}	0.5
Water activity ($\lambda_{a=1}$)	9.2
Water content at saturation ($\lambda_{s=1}$)	16.8

1

2

Table 5 The expressions for the source terms used in the governing equations [18],[19][22].

Source term
$S_u = \frac{\mu}{K}\vec{u}$
$S_{H_2} = -\left({}^{M_{H_2}}/_{2F}\right) j_a \quad in\ ACL$
$S_{O_2} = -\left({}^{M_{O_2}}/_{4F}\right) j_c \quad in\ CCL$
$S_{H_2o} = -\frac{n_d j}{F} M_{H_2o} \quad in\ ACL$
$S_{H_2o} = \frac{n_d j}{F} M_{H_2o} + \left({}^{M_{H_2o}}/_{2F}\right) j_c \quad in\ CCL$
$S_c = \begin{cases} = -j_a & in\ ACL \\ = +j_c & in\ CCL \end{cases}$
$S_m = \begin{cases} = +j_a & in\ ACL \\ = -j_c & in\ CCL \end{cases}$
$S_T = \begin{cases} \frac{i_s^2}{\sigma_{sol}} - S_{gl} & in\ GDLs \\ j_a\left(\eta_a - \frac{T\Delta S_a}{2F}\right) + \frac{i_s^2}{\sigma_{sol}} + \frac{i_s^2}{\sigma_{mem}} - \left(S_{ld} + S_{gl}\right)\cdot L & in\ ACL \\ j_c\left(\eta_c - \frac{T\Delta S_c}{2F}\right) + \frac{i_s^2}{\sigma_{sol}} + \frac{i_s^2}{\sigma_{mem}} - \left(S_{ld} + S_{gl}\right)\cdot L & in\ CCL \\ \frac{i_s^2}{\sigma_{mem}} & in\ CCs \\ 0 & in\ channels \end{cases}$
$S_\lambda = \frac{j_c}{2F} M_{H_2o} \quad in\ CCL$
$S_{gd} = (1-s)\gamma_a M_{H_2o}\frac{\rho_m}{EW}(\lambda^{eq} - \lambda) \quad in\ membrane, ACL\ and\ CCL$
$S_{ld} = s\gamma_{ld} M_{H_2o}\frac{\rho_m}{EW}(\lambda^{eq} - \lambda) \quad in\ membrane, ACL\ and\ CCL$
$\lambda^{eq} = 0.3 + 6a(1 - \tanh(a - 0.5) + 0.69(\lambda_{a=1} - 3.52)a^{0.5}\cdot(1 + \tanh\left(\frac{a - 0.89}{0.23}\right) + s(\lambda_{s=1} - \lambda_{a=1}))$
$S_{gl} = \begin{cases} \gamma_{gl}\varepsilon s D_{gl}\frac{M_{H_2o}}{RT} p \ln\frac{p - p_{sat}}{p - p_{wv}} & p_{wv} \le p_{sat} \\ \gamma_{gl}\varepsilon(1-s) D_{gl}\frac{M_{H_2o}}{RT} p \ln\frac{p - p_{sat}}{p - p_{wv}} & p_{wv} > p_{sat} \end{cases}$
$D_{gl} = \begin{cases} 0.365\cdot 10^{-4}\left(\frac{T}{343}\right)^{2.334}\left(\frac{10^5}{p}\right) & in\ ACL \\ 1.79\cdot 10^{-4}\left(\frac{T}{343}\right)^{2.334}\left(\frac{10^5}{p}\right) & in\ CCL \end{cases}$

Table 6 The boundary conditions used in the simulation model [23][19][22].

Parameter	Value
Mass flow rate of hydrogen	5.55×10^{-8} Kg/s
Mass flow rate of air	5.55×10^{-7} Kg/s
Mass fraction for H_2 at anode inlet	0.144
Mass fraction for H_2O at anode inlet	0.856
Mass fraction for O_2 at cathode inlet	0.242
Mass fraction for H_2O at cathode inlet	0.103
Cathode/anode relative humidity	100%
Temperature at the channel inlets	353 K

Table 7 The pressure drop, temperature difference along the cathode channel and water concentration at the cathode channel exit for the investigated cases.

Cross-section shape	Pressure drop along cathode channel (Pa)	Temperature difference (°C)	Water concentration at channel exit (kmol/m³)
Rectangular	13.3	0.17	0.0138
Trapezoidal	15.1	0.20	0.0151
Hybrid	19.0	0.22	0.0154